

# **ELECTROSPRAY OF 1-BUTYL-3-METHYLIMIDAZOLIUM DICYANAMIDE UNDER VARIABLE FLOW RATE OPERATIONS (POSTPRINT)**

**Benjamin Prince, et al.**

**27 June 2014**

**Interim Report**

**APPROVED FOR PUBLIC RELEASE; DISTRIBUTION IS UNLIMITED.**



**AIR FORCE RESEARCH LABORATORY  
Space Vehicles Directorate  
3550 Aberdeen Ave SE  
AIR FORCE MATERIEL COMMAND  
KIRTLAND AIR FORCE BASE, NM 87117-5776**

## **DTIC COPY NOTICE AND SIGNATURE PAGE**

Using Government drawings, specifications, or other data included in this document for any purpose other than Government procurement does not in any way obligate the U.S. Government. The fact that the Government formulated or supplied the drawings, specifications, or other data does not license the holder or any other person or corporation; or convey any rights or permission to manufacture, use, or sell any patented invention that may relate to them.

This report was cleared for public release by the 377 ABW Public Affairs Office and is available to the general public, including foreign nationals. Copies may be obtained from the Defense Technical Information Center (DTIC) (<http://www.dtic.mil>).

AFRL-RV-PS-TR-2015-0071 HAS BEEN REVIEWED AND IS APPROVED FOR PUBLICATION IN ACCORDANCE WITH ASSIGNED DISTRIBUTION STATEMENT.

//SIGNED//

---

Dr. Raymond Bemish  
Project Manager, AFRL/RVBXT

//SIGNED//

---

Glenn M. Vaughan, Colonel, USAF  
Chief, Battlespace Environment Division

This report is published in the interest of scientific and technical information exchange, and its publication does not constitute the Government's approval or disapproval of its ideas or findings.

Approved for public release; distribution is unlimited.

REPORT DOCUMENTATION PAGE			Form Approved OMB No. 0704-0188		
Public reporting burden for this collection of information is estimated to average 1 hour per response, including the time for reviewing instructions, searching existing data sources, gathering and maintaining the data needed, and completing and reviewing this collection of information. Send comments regarding this burden estimate or any other aspect of this collection of information, including suggestions for reducing this burden to Department of Defense, Washington Headquarters Services, Directorate for Information Operations and Reports (0704-0188), 1215 Jefferson Davis Highway, Suite 1204, Arlington, VA 22202-4302. Respondents should be aware that notwithstanding any other provision of law, no person shall be subject to any penalty for failing to comply with a collection of information if it does not display a currently valid OMB control number. <b>PLEASE DO NOT RETURN YOUR FORM TO THE ABOVE ADDRESS.</b>					
1. REPORT DATE (DD-MM-YYYY) 27-06-2014		2. REPORT TYPE Interim Report		3. DATES COVERED (From - To) 30 Jul 2012 – 27 June 2014	
4. TITLE AND SUBTITLE  ELECTROSPRAY OF 1-BUTYL-3-METHYLIMIDAZOLIUM DICYANAMIDE UNDER VARIABLE FLOW RATE OPERATIONS (POSTPRINT)			5a. CONTRACT NUMBER		
			5b. GRANT NUMBER		
			5c. PROGRAM ELEMENT NUMBER 61102F		
6. AUTHOR(S) Benjamin Prince, Raymond Bemish, Shawn Miller, and Josh L. Rovey			5d. PROJECT NUMBER 2301		
			5e. TASK NUMBER PPM00004270		
			5f. WORK UNIT NUMBER EF004373		
7. PERFORMING ORGANIZATION NAME(S) AND ADDRESS(ES) Air Force Research Laboratory Space Vehicles Directorate 3550 Aberdeen Avenue SE Kirtland AFB, NM 87117-5776			8. PERFORMING ORGANIZATION REPORT NUMBER  AFRL-RV-PS-TR-2015-0071		
9. SPONSORING / MONITORING AGENCY NAME(S) AND ADDRESS(ES)			10. SPONSOR/MONITOR'S ACRONYM(S) AFRL/RVBXT		
			11. SPONSOR/MONITOR'S REPORT NUMBER(S)		
12. DISTRIBUTION / AVAILABILITY STATEMENT  Approved for public release; distribution is unlimited. (377ABW-2013-0681 dtd 26 Aug 2013)					
13. SUPPLEMENTARY NOTES  Accepted for publication in the Journal of Propulsion and Power, 23 Mar 2014. Government Purpose Rights.					
14. ABSTRACT  The ionic liquid 1-butyl-3-methylimidazolium dicyanamide ([Bmim][DCA]) is a propellant candidate for a standalone electrospray thruster or a dual-mode propulsion system. Characterization of positive polarity ions produced by [Bmim][DCA] capillary emitters with a nominal extraction voltage of 2.0 kV is presented, followed by predictions of propulsion performance. Flow rates from 0.27 to 2.18 nL/s are used to investigate the impact variations in the flow parameter have on the electrospray plume. Measurements indicate the presence of Bmim__Bmim__DCA__ <i>n</i> ( <i>n</i> _ 0, 1, 2, 3, 4) cation species plus droplet contributions. At 0.27 nL/s, the <i>n</i> _ 1 species dominates the mass spectrum contributing 56.5% of the total intensity, while at 2.18 nL/s, the dominant species is <i>n</i> _ 4, comprising 40.7%. Based on the retarding potential analysis, ions emitted from the capillary are formed below the emitter potential of 500 eV. Angular distributions indicate the broadening of both the beam current and mass distribution for increasing flow rates. As the flow rate increases from 0.30 to 2.18 nL/s, derived thrust and specific impulse change from 0.84 μN and 200 s to 2.90 μN and 80 s, respectively.					
15. SUBJECT TERMS  Ionic liquid, electrospray thruster, capillary emitter, electrospray plume					
16. SECURITY CLASSIFICATION OF:			17. LIMITATION OF ABSTRACT  Unlimited	18. NUMBER OF PAGES  16	19a. NAME OF RESPONSIBLE PERSON Dr. Raymond Bemish
a. REPORT Unclassified	b. ABSTRACT Unclassified	c. THIS PAGE Unclassified			19b. TELEPHONE NUMBER (include area code)

This page is intentionally left blank.

# Electrospray of 1-Butyl-3-Methylimidazolium Dicyanamide Under Variable Flow Rate Operations

Shawn W. Miller,<sup>\*</sup> Benjamin D. Prince,<sup>†</sup> and Raymond J. Bemish<sup>‡</sup>  
*U.S. Air Force Research Laboratory, Kirtland Air Force Base, New Mexico 87117*  
and  
Joshua L. Rovey<sup>§</sup>  
*Missouri University of Science and Technology, Rolla, Missouri 65409*

DOI: 10.2514/1.B35170

The ionic liquid 1-butyl-3-methylimidazolium dicyanamide ([Bmim][DCA]) is a propellant candidate for a standalone electrospray thruster or a dual-mode propulsion system. Characterization of positive polarity ions produced by [Bmim][DCA] capillary emitters with a nominal extraction voltage of 2.0 kV is presented, followed by predictions of propulsion performance. Flow rates from 0.27 to 2.18 nL/s are used to investigate the impact variations in the flow parameter have on the electrospray plume. Measurements indicate the presence of Bmim([Bmim][DCA])<sub>n</sub><sup>+</sup> ( $n = 0, 1, 2, 3, 4$ ) cation species plus droplet contributions. At 0.27 nL/s, the  $n = 1$  species dominates the mass spectrum contributing 56.5% of the total intensity, while at 2.18 nL/s, the dominant species is  $n = 4$ , comprising 40.7%. Based on the retarding potential analysis, ions emitted from the capillary are formed below the emitter potential of 500 eV. Angular distributions indicate the broadening of both the beam current and mass distribution for increasing flow rates. As the flow rate increases from 0.30 to 2.18 nL/s, derived thrust and specific impulse change from 0.84  $\mu$ N and 200 s to 2.90  $\mu$ N and 80 s, respectively.

## Nomenclature

$F$	=	thrust, N
$G$	=	acceleration of gravity, $\text{m/s}^2$
$I$	=	total beam current, A
$I_{\text{sp}}$	=	specific impulse, s
$K$	=	ionic liquid electrical conductivity, S/m
$\dot{m}$	=	total mass flow rate, kg/s
$m/q$	=	mass-to-charge ratio, amu/e
$P_e$	=	electrical power, W
$P_0$	=	reservoir pressure, torr
$Q$	=	ionic liquid volumetric flow rate, nL/s
$q/m$	=	specific charge, C/kg
$V_{\text{acc}}$	=	acceleration potential, V
$V_{\text{ext}}$	=	extractor plate potential, V
$V_N$	=	emitter potential, V
$v$	=	propellant ejection velocity, m/s
$V_{\Omega}$	=	potential due to ohmic losses, V
$\gamma$	=	ionic liquid surface tension, N/m
$\epsilon$	=	ionic liquid dielectric constant
$\epsilon_0$	=	permittivity of free space, F/m
$\mu$	=	ionic liquid viscosity, cP
$\rho$	=	ionic liquid density, $\text{kg/m}^3$

## I. Introduction

ELECTROSPRAY thrusters are a class of microelectric propulsion systems that field evaporate a conductive liquid propellant. Liquid flows to the tip of the electrospray emitter where a strong electric field is present. Under the right conditions of the flow rate and field strength, a cone structure (i.e., Taylor cone [1]) develops at the tip of the emitter. This cone results from the balance between the pull of the surface tension of the liquid and of the applied electric field. Two ion emission zones have been proposed for the Taylor cone (see Fig. 1) [2–5]. The first zone is at the transition region between the cone and jet structure known as the neck. The second zone occurs at the jet breakup region located at the jet tip. Along with small ions, larger charged masses have been detected from this second emission zone. Early studies of electrospray (also termed colloid) thrusters used glycerol or salt solutions as propellants. More recently, the choice propellants are molten salts known as ionic liquids (ILs), specifically, room-temperature ionic liquids [6,7]. A common IL frequently used in electrospray research has been 1-ethyl-3-methylimidazolium bis(trifluoromethylsulfonyl)imide ([Emim][Im]), which has a conductivity of 0.92 Siemens per meter (S/m) and a viscosity of 32.6 centipoise (cP) at 298 K [8]. These properties facilitate ion extraction at low voltages (i.e., <3 kV) in a single cone-jet mode.

In this paper, we focus on another IL, 1-butyl-3-methylimidazolium dicyanamide ([Bmim][DCA]), that has received less attention as an electrospray propellant under controlled-variable flow rate operation. Interest in [Bmim][DCA] stems from its potential to serve as both a chemical propulsion and electrospray propellant, enabling what is called a dual-mode or multimode propulsion system. [Bmim][DCA] exhibits physical properties (see Table 1) similar to [Emim][Im], including an ease of electrospraying [9–15]. Additionally, the heat of formation of [Bmim][DCA] is double that of hydrazine (206.2 vs 109.3 kJ/mol for hydrazine), making it a potential candidate for chemical propulsion [16]. Experimental and numerical studies have explored the use of [Bmim][DCA] in chemical engine applications. Schneider et al. [17] studied a variety of liquids with fuel-rich anions, which included liquids with the dicyanamide anion. The study found [Bmim][DCA] to be hypergolic with white fuming nitric acid, resulting in an ignition delay time of 47 ms, longer than the desired maximum of 5 ms. Numerical predictions by Berg and Rovey [18,19] suggest that pure [Bmim][DCA] has a 20% lower specific impulse than hydrazine but that a binary combination of [Bmim][DCA] with hydroxylammonium nitrate (HAN) oxidizer may equal or exceed

Presented as Paper 2012-3738 at the 48th AIAA/ASME/SAE/ASEE Joint Propulsion Conference & Exhibit, Atlanta, GA, 30 July–1 August 2012; received 10 September 2013; revision received 12 February 2014; accepted for publication 23 March 2014; published online 27 June 2014. This material is declared a work of the U.S. Government and is not subject to copyright protection in the United States. Copies of this paper may be made for personal or internal use, on condition that the copier pay the \$10.00 per-copy fee to the Copyright Clearance Center, Inc., 222 Rosewood Drive, Danvers, MA 01923; include the code 1533-3876/14 and \$10.00 in correspondence with the CCC.

<sup>\*</sup>Graduate Student, Mechanical and Aerospace Engineering, 160 Toomey Hall, 400 West 13th Street. Student Member AIAA.

<sup>†</sup>Research Chemist, Space Vehicles Directorate, 3550 Aberdeen Building 570. Member AIAA.

<sup>‡</sup>Senior Research Chemist, Space Vehicles Directorate, 3550 Aberdeen Building 570.

<sup>§</sup>Assistant Professor of Aerospace Engineering, Mechanical and Aerospace Engineering, 292D Toomey Hall, 400 West 13th Street. Senior Member AIAA.

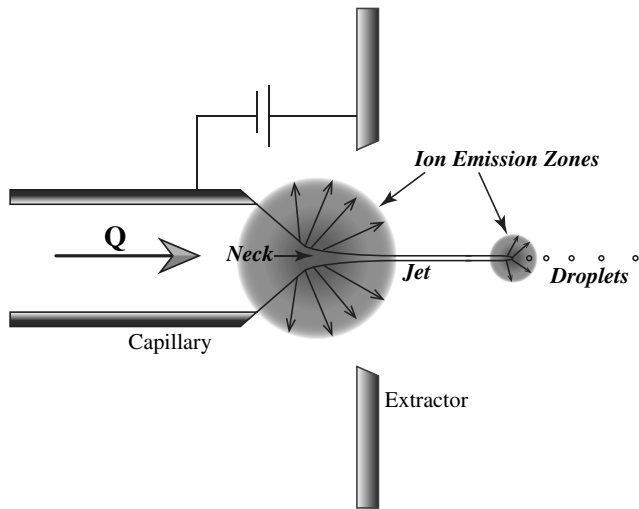


**Fig. 1 Taylor cone structure and ion emission zones of a capillary emitter.**

hydrazine performance. Additionally, spacecraft models by Donius and Rovey [20,21] show that mass savings through a common propellant for a dual-mode system more than offset the mass penalty associated with lower performance.

An option for expanding the capability of a capillary electrospray emitter is the use of controlled-variable flow rate operations. While this control method has been known for some time, there has been limited research on its implementation and the independent effect of the flow rate on electrospray operation. Cloupeau and Prunet-Foch [22] conducted the earliest direct flow control while studying electrospray operating modes and cone-jet mode sprays. These investigations focused on varying electrospray parameters to determine the effect on the observable emission modes (e.g., jet geometry). They investigated how voltage, beam current, and droplet frequency depended on flow rate. The studied flow rate range was 1.0 nanoliters per second (nL/s) to 10 microliters per second for liquids of various conductivities. Gamero-Castaño and Hruby [23] studied the effect of flow rate on beam current and, ultimately, thrust and  $I_{sp}$ . The flow rate was also compared to the flux measured by time-of-flight techniques. For [Emim][Im] emitted at the two flow rates of 0.36 and 0.14 nL/s, beam current and  $I_{sp}$  changed from 307 nA and 126 s to 216 nA and 171 s as thrust output dropped from 0.628 to 0.352  $\mu$ N. Romero-Sanz et al. [6] later conducted a flow controlled experiment for the IL 1-ethyl-3-methylimidazolium tetrafluoroborate ([Emim][BF<sub>4</sub>]) similar to the [Bmim][DCA] study that follows in which a range of backing pressures was explored: 28 to 2310 torr. Only the three smallest cations (i.e., Emim<sup>+</sup>, Emim([Emim][BF<sub>4</sub>])<sup>+</sup>, and Emim([Emim][BF<sub>4</sub>])<sub>2</sub><sup>+</sup>) were distinguishable in the data and were assigned associated currents at each pressure setting. The remaining current that could not be assigned to the small cations was classified as droplet contribution. This droplet contribution consists of all charged species of greater mass than the three cations. For each of the three cations, the current increased to a maximum then decreased as pressure increased, while the current of the droplet contribution increased over the entire pressure range. These current vs pressure trends suggest a beam composition change as a function of flow rate.

In this study, we investigate emission of the IL [Bmim][DCA] from an internal flow capillary and characterizes the [Bmim][DCA] electrospray plume. Experimental results are then used to predict the electrospray propulsion performance of [Bmim][DCA]. By characterizing the plume and predicting performance, the aim is to

determine the variability and tunability of the electrospray plume to specific ion emission products and thus specific propulsion performance levels through flow rate adjustment.

## II. Experiment

To predict the electrospray performance, it is necessary to measure the current and mass flow rate. Additionally, the ion mass intensities and kinetic energies are measured to ascertain the electrospray beam composition. These measurements are accomplished using the angle-resolved technique detailed by Chiu et al. [24,25]. This technique is chosen over the time-of-flight (TOF)/stopping potential approach due to improved resolution in identifying the ionic species (or  $m/q$  ratio) produced in the electrospray cone-jet operation mode and collection of complementary TOF information. In addition, this apparatus is relatively insensitive to the ion energy distribution and allows for energy distribution measurements of the mass-resolved ionic species. To establish the impact of beam divergence, the technique incorporates the measurement of the angular distribution of emitted charged species. These measurements can provide an assessment on such considerations as thrust cosine losses, spacecraft integration and exhaust contamination, operating conditions, and identification of ion emission regions.

### A. Apparatus

Figure 2 is a schematic diagram of the experimental setup used for the angle-resolved quadrupole mass spectrometric analysis [9,24,25]. The setup consists of three sections: rotating emission source, near-field targets, and far-field targets. The rotatable emission source is an internal flow capillary attached to a rotation stage allowing the angle of the spray to be varied with respect to the experimental axis. The source framework supports both an electrified extractor plate and the electrospray emitter. A 1.5-mm-diameter orifice in the extractor plate allows for the passage of the electrospray plume.

Near-field targets are mounted on a translating stage and consist of a Faraday cup, quartz crystal microbalance [(QCM); model XTM/2 supplied by Inficon], and a cylindrical electrostatic lens element. These are 18 mm downstream from the emission source. The Faraday cup and QCM measure the current and mass flow rate of the electrospray beam. Equal-sized apertures with 0.8 mm diameters are used on both targets. The aperture diameters, with a measurement interval of 2.5 deg, minimize oversampling. When the cylindrical electrostatic lens element is moved into the electrospray beam path, the electrospray beam can continue onward to the far-field targets: a quadrupole mass filter with a set of focusing lenses at the entrance, a set of three grids used for the retarding potential analysis (RPA), and an off-axis channeltron detector. The channeltron detector is the signal collector for the mass spectrometric or RPA measurements in the far field. The mass filter selects specific ion masses for the channeltron detector, while the RPA establishes the ion kinetic energy. The RPA operates by determining the potential required to block the ions from reaching the channeltron detector.

### B. Charged Emission Sources

A capillary needle emitter is used for all experiments. The emitter and extractor geometry are shown schematically in Fig. 1. The capillary needle has an internal flow of the IL that is dependent on the backing pressure of the fluid feed system, depicted in Fig. 3. The reservoir pressure  $P_0$  provides a backing pressure on the IL. This constant pressure is maintained by admitting an inert gas (in this case nitrogen) into the reservoir and pumping with a mechanical pump. The needle valve allows for direct control and setting of the reservoir

**Table 1 Physical properties of the IL [Bmim][DCA] compared to [Emim][Im] at 298 K**

Ionic liquid	Formula	K, S/m	$\mu$ , cP	$\rho$ , kg/m <sup>3</sup>	$\gamma$ , N/m	$\epsilon$
[Bmim][DCA]	C <sub>10</sub> H <sub>15</sub> N <sub>5</sub>	1.052 [10]	33.2 [11]	1063.1 [11]	0.0486 [12]	11.3 [13]
[Emim][Im]	C <sub>8</sub> H <sub>11</sub> F <sub>6</sub> N <sub>3</sub> O <sub>4</sub> S <sub>2</sub>	0.92 [8]	32.5 [8]	1519.3 [14]	0.0357 [14]	12.3 [15]

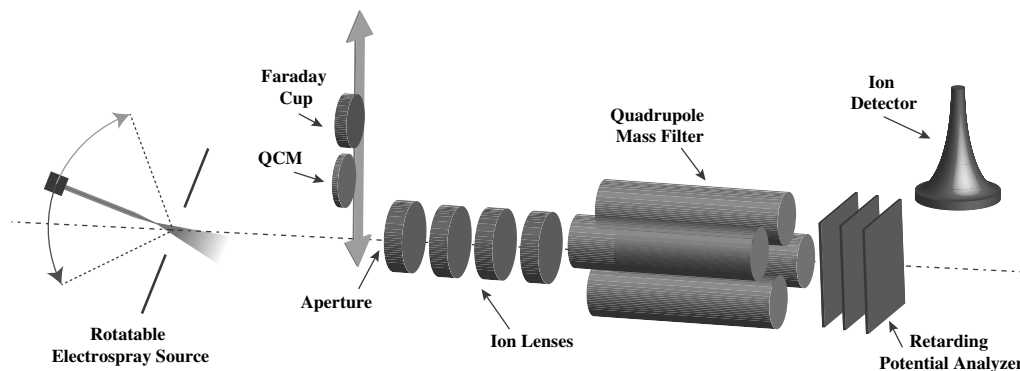


Fig. 2 Experimental setup.

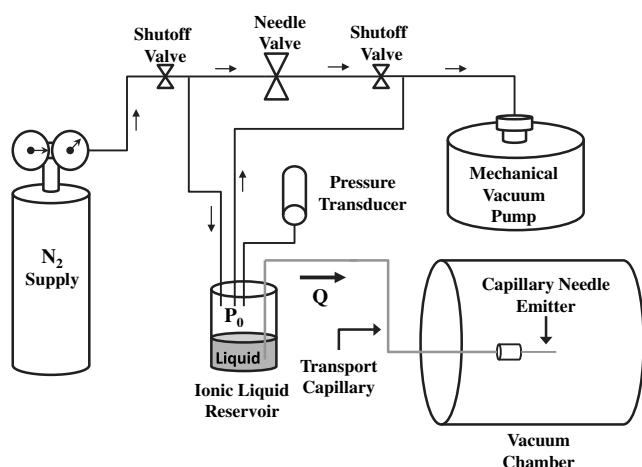


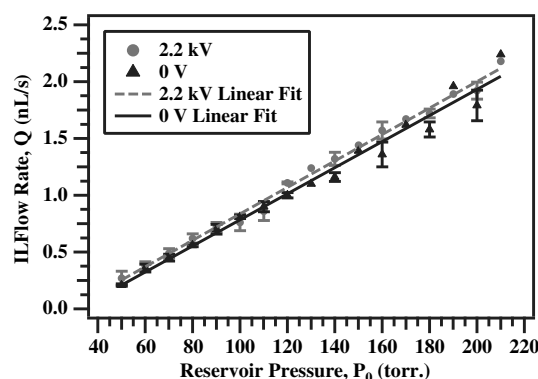
Fig. 3 Capillary fluid feed system. Arrows indicate flow path of gas.

pressure in small pressure increments. The IL is fed by the fluid feed system from a reservoir, through a transport capillary, and out the tip of the capillary needle emitter. The transport capillary is fused silica with a  $100\ \mu\text{m}$  inner diameter (ID) and an  $82.5\ \text{cm}$  length. The capillary needle is stainless steel with a tapered tip of  $50\ \mu\text{m}$  inner diameter and  $3.5\ \text{cm}$  length. Both capillaries are commercially available. This feed system is similar to the system used by Lozano [26], but the direct monitoring of the reservoir pressure using a pressure transducer eliminates the need to calculate the reservoir pressure based on the regulated source gas or pumping speed of the mechanical vacuum pump. When not in use, the ionic liquid reservoir remains under rough vacuum ( $<100\ \text{torr}$ ) to prevent water absorption.

### C. Flow Rate Calibration

The reservoir pressure  $P_0$  is dependent on the nitrogen supply pressure, vacuum pumping speed, and length of gas transport lines of the setup. By expressing data as a function of the volumetric flow rate, the results are independent of the specific capillary fluid feed system. Experiments with other feed systems can therefore be directly compared with results presented here for the equivalent flow rate, assuming that the same capillary tip inner diameter is used. To measure the flow rate, a bubble of nitrogen is introduced into the capillary, and its velocity is measured using a visual magnifier giving a direct measure of the IL flow rate at various  $P_0$  conditions. For the data collected, the velocity is measured in the transport capillary, external of the vacuum chamber.

Figure 4 shows the calibration results of two experimental sets of data collected at the two voltage conditions of  $0\ \text{V}$  and  $2.2\ \text{kV}$ . Both data sets have a linear trend and a maximum difference less than  $11\%$ . The average values, with a standard deviation of less than  $9\%$ , are shown in Fig. 4. Based on the trend and correlation between data points, the presence of the electric field does not appear to influence the IL volumetric flow rate as measured in the transport capillary.

Fig. 4 Comparison of IL flow rate vs reservoir pressure  $P_0$ .

When the bubble results are compared to the mass flow rate based on QCM measurements, the QCM values are larger and represent a  $25\%$  systematic increase over the bubble method. The nominal capillary diameter is used to calculate the bubble method flow rate. The conclusion is that the difference in the two flow rates is merely due to a manufacturing tolerance. This difference translates to a required  $12\%$  increase in the capillary radius (i.e., actual radius of  $28\ \mu\text{m}$ , not  $25\ \mu\text{m}$ ) to obtain the QCM flows. The QCM measurements are not used for calibration since full mass flow collection is not possible for all flow rate conditions.

### III. Plume Analysis Results

The plume analysis was conducted for a capillary emitter and extractor set with an extraction potential of  $2.0\ \text{kV}$  ( $V_N = +500\ \text{V}$ ,  $V_{\text{ext}} = -1500\ \text{V}$ ). In this simple two-electrode geometry, the theoretical acceleration  $V_{\text{acc}}$  is equivalent to the potential extraction potential (i.e.,  $V_{\text{acc}} = V_N - V_{\text{ext}}$ ). However, ohmic losses occur within the jet structure of the Taylor cone reducing the potential of the emitted ions and leading to a reduced acceleration potential. This means the actual acceleration potential is  $V_{\text{acc}} = V_N - V_{\text{ext}} - V_{\Omega}$ . When the acceleration potential is used to calculate thrust values in the remainder of this paper,  $V_{\text{acc}}$  will be  $1793\ \text{V}$  based on the retarding potential analysis results to be discussed. The  $0.8\text{-mm}$ -diameter aperture before the near-field targets is set to ground. Given space limitations between the detectors and the rotatable source, angular measurements were possible only between  $\pm 60^\circ$ .

Figures 5 and 6 illustrate the measured beam current as a function of flow rate but with respect to two different sampling areas. The current density in Fig. 5 is the angular measurement normalized to the detector aperture area. The maximum current density per flow rate is maintained at  $0^\circ$  (on axis), but the current profiles broaden as the flow rate increases. At the highest flow rates, the current density profile approaches the acceptance angle limitation of the extractor aperture ( $\sim 56^\circ$ ) resulting in the profile cutoff. The maximum measured current density of  $2.09\ \text{nA} \cdot \text{mm}^{-2}$  is observed at  $0^\circ$  for a flow rate of  $0.30\ \text{nL/s}$ . With the shift in current to higher angles as

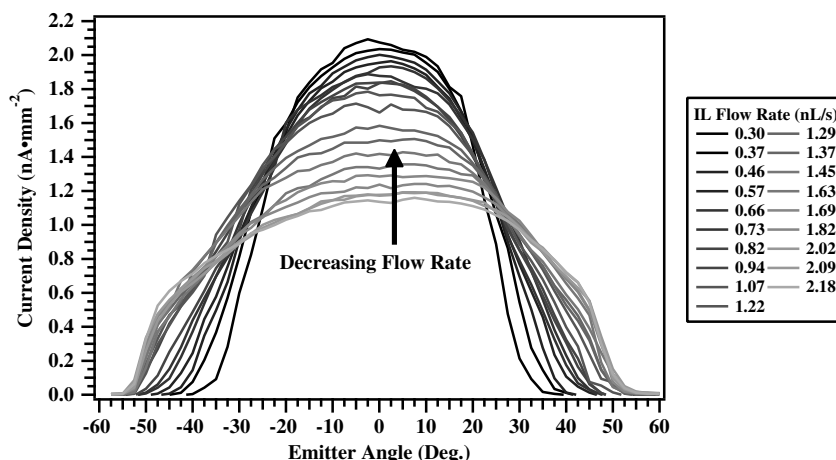


Fig. 5 Capillary plume current density vs emitter angle for discrete IL flow rates.

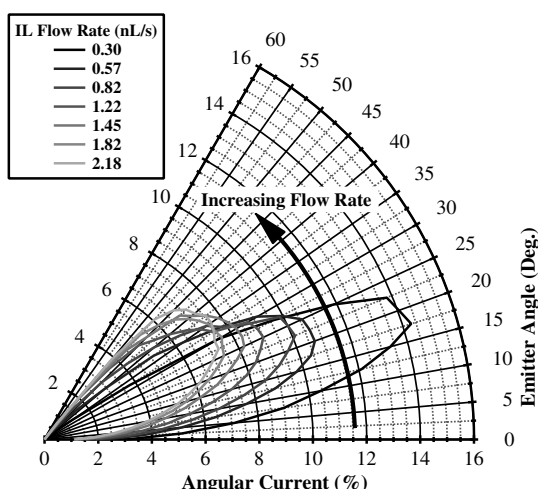


Fig. 6 Select angular current contribution to the integrated beam current.

the flow rate increases, the current density at 0 deg drops to  $1.15 \text{ nA} \cdot \text{mm}^{-2}$  for the maximum flow rate,  $2.18 \text{ nL/s}$ . The redistribution of current is best observed in the polar plot (Fig. 6) of the angular current contribution. In this current plot, the sampling area varies as a ring of the integrated current hemisphere. Each ring has the circumference at the given angle on the hemisphere and a width of  $0.85 \text{ mm}$ , the sine component for a  $2.5 \text{ deg}$  step size between each measurement. The angular current contribution is a percentage normalized by the total integrated current for each flow rate. Unlike the current density profiles, the peak current does not occur at 0 deg for any of the flow rates studied. At  $0.30 \text{ nL/s}$ , the current percentage peaks at  $17.5 \text{ deg}$ , and as the flow rate increases, the peak value shifts toward higher angles. The highest angle of current emission occurs at  $35 \text{ deg}$ . The shifting maximum current percentage indicates that emission occurs less along 0 deg and more toward the perpendicular direction. If the current were centered on 0 deg, then most of the emission would be parallel to the electrospray beam axis.

Similar to the current density trends, the mass flow rate trends (Fig. 7) indicate mass redistribution occurring as the IL flow rate increases for the same angular measure and fixed aperture area. However, unlike the current density, the centerline mass flow rate value continues to increase as the high angle values increases. The maximum mass flow at  $0.30 \text{ nL/s}$  is  $2.35 \text{ ng} \cdot \text{mm}^{-2} \cdot \text{s}^{-1}$ . The  $m/q$  of the capillary at  $0.30 \text{ nL/s}$  is  $90,000 \text{ atomic mass unit (amu)}$  or equivalent to an IL cluster of  $n = 439$ , determined from the integration of the available QCM and Faraday cup data and assuming singly charged particles. In contrast, the highest IL flow rate,  $2.18 \text{ nL/s}$ , generates a flow of  $9.11 \text{ ng} \cdot \text{mm}^{-2} \cdot \text{s}^{-1}$  and a  $m/q$  of  $566,000 \text{ amu}$  (i.e.,  $n = 2761$ ). This peak value of mass flow is nearly

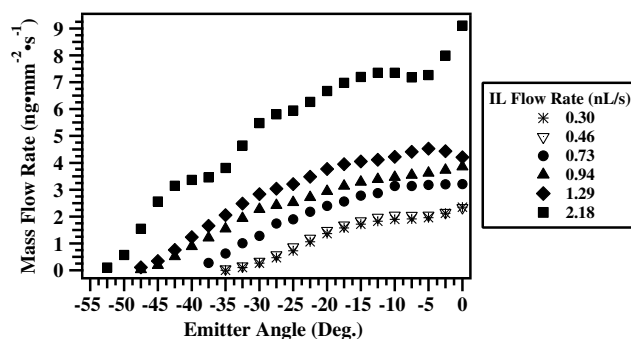


Fig. 7 Mass flow rate vs emitter angle for various IL flow rates.

12 times larger than the value associated with the more typical etched metal needle IL emitters. Typically for a metal needle, the peak mass flow rate is approximately  $0.71 \text{ to } 1.06 \text{ ng} \cdot \text{mm}^{-2} \cdot \text{s}^{-1}$  [9,25]. Achieving a higher mass flow rate as the IL flow rate increases is not surprising since, by conservation of mass, the mass flow rate scales to the volumetric flow rate by the IL density.

Mass flow rate data points are collected at intervals of  $5 \text{ deg}$  and then interpolated for the angles in between for the IL flow rates illustrated in Fig. 7. The  $5 \text{ deg}$  angle interval is used to prolong the accuracy of the QCM. Since  $[\text{Bmim}][\text{DCA}]$  has a low vapor pressure and does not vaporize under vacuum, any liquid collected on the surface of the QCM remains on the surface. At flow rates above  $0.72 \text{ nL/s}$ , the crystal frequency rapidly decreases from the nominal  $6 \text{ MHz}$ . This result is attributed to the high rate of deposition of the IL mass on the crystal surface, which invalidates the thin film assumption. Cleaning the crystal of the IL deposit restores the QCM operation until the IL builds up again. Consistent, repeatable results are only obtainable when the IL deposit layer is not significant and the crystal frequency remains higher than  $5.9 \text{ MHz}$ . This challenge has not been observed with externally wetted needle emitters with a much lower mass flow rate [25,27].

To verify that the Faraday cup fully captures the output of the capillary, the currents on the capillary tip and the extractor plate, hereafter referred to as the emitter current and extractor current, are obtained by measuring the potential across a  $4.93 \text{ M}\Omega$  equivalent resistance on each associated voltage line and applying Ohm's law. This emitter current can be compared to the integrated results of the current density profiles in Fig. 5. The integrated beam current is calculated by integrating each current density profile over a hemisphere, similar to the Hall thruster beam current analysis of Manzella and Sankovic [28]. However, unlike their work in which the ratio between the detector distance to detector aperture size is  $\sim 20:1$ , the ratio for the current experiment is  $\sim 25:1$ .

With an IL capillary electrospray setup, a completed circuit can be achieved from both the electrospray tip and the IL reservoir. As a



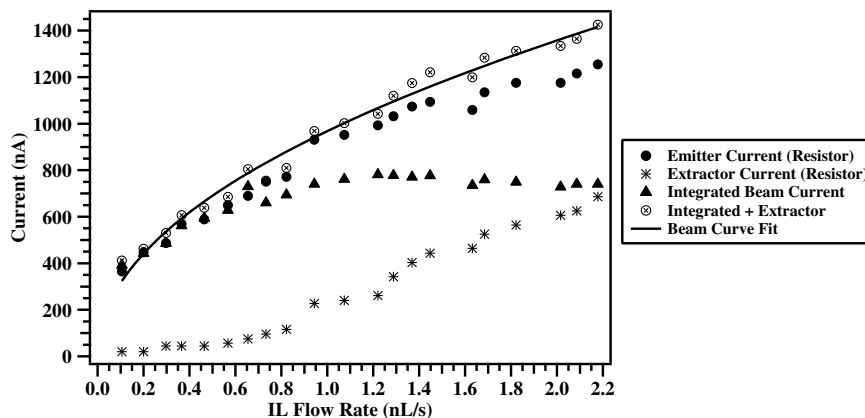


Fig. 8 Emission current as a function of the IL flow rate.

result, the IL reservoir must be insulated so that only the electrical circuit from the capillary tip exists. No emitter potential should be present when electrode potentials are applied on an IL filled capillary with no reservoir backing pressure. If a potential is detected, then a current path is present in the IL reservoir. The extractor plate is the closest point to the capillary tip for establishing an additional current path other than the Faraday cup. An increase in the extractor current will correspondingly appear as a reduction in the integrated current when the circuit path is connected.

Figure 8 shows the emission current results of a 50  $\mu\text{m}$  stainless-steel tip over the same IL flow rate range as Fig. 5. The emitter current is between 375 and 1200 nA. Full current recovery is achieved only by adding the results of the integrated current and extractor current together. This recovery indicates only the extractor is an additional current path and a significant source of current loss for IL flow rates over 0.90 nL/s. The integrated current over 0.90 nL/s accounts for 60 to 90% of the emitter current, but that percentage coincides with the mass flux accounted for by the QCM. The QCM measurement represents nearly 99% of the total mass supplied by the capillary, indicating most of the charge is not carried by the bulk of the emitted mass. Instead, the remaining 10 to 40% of the emission current is carried by low-mass ions (discussed in the following), representing 0.5% of the total mass, and is emitted outside the angle range measured. The detected charge distributed over the associated mass at a given flow rate results in an average  $m/q$  ranging from 90,000 (at 0.30 nL/s) to 566,000 amu (at 2.18 nL/s), assuming singly charged species.

The far-field measurements are presented for the three selected volumetric flow rates of 0.27, 1.24, and 2.18 nL/s per the angular measurement, not integrated over the hemispherical area. The measured mass intensities (arbitrary units, arb.) are assembled into the mass spectra of Fig. 9 and [Bmim][DCA] cations assigned to each set of peaks. Table 2 lists the relevant cations and associated masses within the detection range of the mass filter. The angle-resolved mass spectra are presented at two different intensity scales in Fig. 9 since at high volumetric flow rates the identifiable ions occur at a reduced intensity. To maintain comparability, the same voltage settings are used on the channeltron detector for all mass spectra and RPA data. This allows a relative comparison between the data sets of each flow rate. Kinetic energy profiles are presented in Figs. 10–12 at centerline (i.e., on axis) and at 17.5 deg (i.e., off axis). In conducting the RPA scans, the four sampled masses, 344, 754, 800, and  $m/q > 1000$  amu are used to establish the kinetic energy profiles. The first two masses represent cations at the low and high ends of the mass filter range. The 800 amu setting is used as a background measurement and is subtracted from the measurements of the cations. For  $m/q > 1000$  amu, this is an all-pass scan, which allows any mass greater than 1000 amu to pass through the mass filter and into the RPA grids. The all-pass scan indicates the presence of larger masses not detected by the mass spectrometric measurements.

The mass spectra results (Fig. 9) show that all cation species in the quadrupole mass range (Bmim([Bmim][DCA]) $_n^+$  for  $n = 0, 1, 2, 3, 4$ ) are present; although under increasing flow rate conditions, the

intensity of these species decreases. No evidence of multiply charged species or fragmentation of the parent cation is observed in the mass spectra. Cation species less than 500 amu only occur in trace amounts (i.e., <10% of the total intensity) at higher flow rates. The mass intensity of each detected species becomes uniform across the angle measurement range as the flow rate increases. In addition to the mass spectra, the mass intensity per ion emission product has been integrated, establishing a percent contribution of each emission product, excluding  $m/q > 1000$  amu. Table 3 lists the percent contribution of the measured intensity of each ion species over the flow rate and angle. The dominant species for 0.27 nL/s is (Bmim([Bmim][DCA]) $_1^+$ , which contributes 56.5% of the measured intensity. As the IL flow rate increases, the dominant species transitions to (Bmim([Bmim][DCA]) $_4^+$  contributing 40.7% of the measured intensity at 2.18 nL/s. Note that the percentages are for the measured intensities within the range of 0–1000 amu. These percentages do not account for the droplet proportion of the beam since such large masses cannot be measured by the mass spectrometer.

Figures 10–12 show the energy distribution measured by the RPA at two different angles (0 and 17.5 deg). The maximum value of the distributions indicates the most probable kinetic energy of each ion species and is identified by a vertical line. The distribution trends for each cation species (344, 754, and  $m/q > 1000$  amu) are similar between changes in the flow rate and angle. However, the measured peak value increases with the angle and decreases with pressure. At 0.27 nL/s, a 80 (754 amu) and 50 eV ( $m/q > 1000$  amu) increase in the peak energy occurs between the on- and off-axis cases. At 1.24 and 2.18 nL/s, 70 and 40 eV increases occur between the on- and off-axis cases of the 754 and  $m/q > 1000$  amu emission products, respectively. The maximum energies of each distribution are less than 400 eV and well under the 500 eV emitter potential, suggesting that the ions are born at a lower potential than the capillary. The effect increases with flow rate but is less effectual at larger angles. Identifying the source of loss will be an important step in maximizing ion kinetic energy. Surprisingly, the data at all three flow rates indicate a significant presence of mass over 1000 amu within the electrospray beam even at high angles. The  $m/q > 1000$  amu kinetic energy distribution accounts for the high-mass flow rate measurements at high angles even though the mass spectra show minimal mass below 1000 amu at those angles.

#### IV. Discussion

The electrospray cone-jet characteristics do not remain static when the IL flow rate is altered. Instead, the charge distribution, mass distribution, and kinetic energy of the beam modify with the flow rate change. Taken together, these microscopic quantities are the basis for the propulsive performance of the capillary emitter. In the following sections, these electrospray dependencies are discussed based on the exhibited trends in the current density, mass flow rate, mass spectra, and RPA data. When thrust and  $I_{sp}$  are calculated using the near-field results, electrospray performance of a single emitter is established

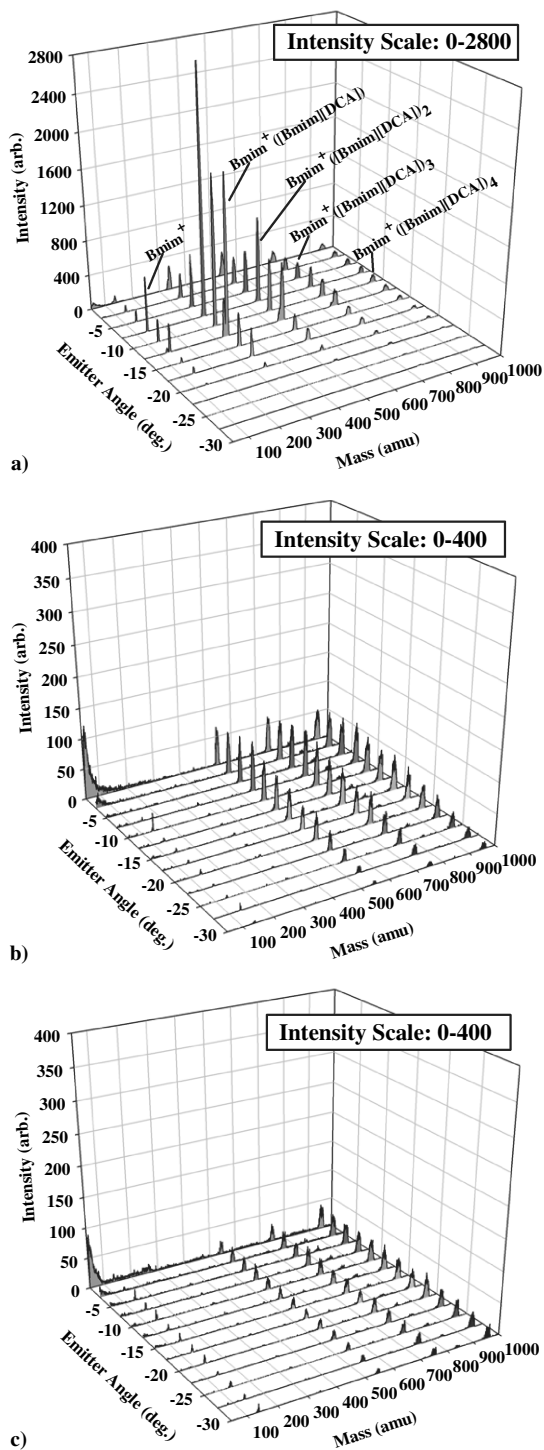


**Fig. 9** Angle-resolved cation mass spectra at flow rates a) 0.27 nL/s, b) 1.24 nL/s, and c) 2.18 nL/s.

and can be connected to the beam characteristics and composition at specific IL flow rates.

## A. Plume Properties

### 1. Beam Profile Changes

The electrospray beam profile significantly changes over the range of IL flow rates sampled. The current profiles in Figs. 5 and 6 indicate a redistribution of charge with the changing flow rate. Increasing flow pushes charged species to larger angles until they extend beyond the limit of the measurement range at 56 deg due to the acceptance angle of the extractor aperture. The mass flow rates shown in Fig. 7 corroborate this broadening. No mass is observed at 37.5 deg from center for the lowest flow rate, while nearly 38% (i.e.,

$3.46 \text{ ng} \cdot \text{mm}^{-2} \cdot \text{s}^{-1}$ ) of the peak value,  $9.11 \text{ ng} \cdot \text{mm}^{-2} \cdot \text{s}^{-1}$ , is observed at the same angle for the highest flow rate examined. The three mass spectra in Fig. 9 mirror this observed behavior. At the lowest flow rates (Fig. 9a), ionic species ( $n < 4$ ) are only detected within roughly 20 deg from the center, while at larger flow rates, ionic species  $n = 2$  to 4 are present in the spectra beyond 20 deg. Table 3 indicates the percent contribution of the measured intensity of each ion species for each IL flow rate over the angle range  $-20$  to  $-30$  deg. For that range, the data indicate a 3 to 20% increase in  $n = 2$  to 4 species as the flow rate changes. At 2.18 nL/s, the measured spectrum (Fig. 9c) appears as a nearly flat distribution peaked along the centerline. The data in Table 3 correlate with this flat distribution as 20% of the measured intensity is contributed to both the 0 to  $-20$  deg and the  $-20$  to  $-30$  deg angle ranges.

In addition to the increasing divergence as the flow rate increases, the compositional makeup of the electrospray plume is significantly affected by the change of the flow rate. At the lowest flow rate studied, the  $n = 1$  species accounts for 56.5% of the measured intensity at this low flow rate. As the flow rate is increased to 2.18 nL/s, the  $n = 4$  species accounts for 40.7% of the measured intensity. Further, the intensities of species in the detection range are decreased by roughly a factor of 50 over those intensities observed at the lowest flow rate. The transition in the dominant species and the decrease in intensity suggest that the beam composition has transitioned to larger charged masses and that greater contribution results from species of  $m/q > 1000$  amu to account for the higher mass flow rates detected by the QCM. The transition in the emission product is corroborated by the change in jet diameter. Fernández de la Mora and Loscertales [29] established that the jet diameter scales as a function of the IL flow rate. When evaluated at 0.27 and 2.18 nL/s, the jet diameters are approximately 15 and 31 nm, respectively. These diameters are determined using the droplet-to-jet-diameter ratio of 1.89 as established by Cloupeau and Prunet-Foch [22] and the droplet diameter equation specified by Gañán-Calvo et al. [30]. The increasing jet diameters suggest that larger droplets are produced, changing the beam composition as the flow rate increases. It should be noted that the stated jet diameters result in jet velocities far greater than 500 eV, which do not appear in the kinetic energy profiles of the RPA. Jet diameters four times these values are necessary to achieve correspondence with the energy profiles. It appears that this experiment does not follow the accepted ratio of 1.89.

### 2. Reduced Ion Energies and Origin Points

The RPA data shown in Figs. 10–12 indicate, for any studied flow rate, that all ions emitted from the capillary are at kinetic energy levels well below the emitter bias potential. In the experiment, emitters are biased to 500 V to maintain ion transmission through the apparatus and to minimize the ion energy in the mass filter [25]. If the energy distribution of a charged species peaks at 500 eV, then it can be concluded that the species originates near the emitter. Otherwise, any substantial energy drop is indicative of ohmic losses. These losses occur as a result of the resistivity of the IL. As current flows through the jet that has a large length-to-cross-sectional-area ratio (i.e., on the order of  $0.3 \text{ nm}^{-1}$ ), Ohm's law takes effect, and the potential is reduced in accordance to the resistance of the jet. The cone does not experience such ohmic losses due to the much smaller length-to-cross-section-area ratio (i.e., less than  $0.01 \text{ nm}^{-1}$ ). The width of the energy distribution is indicative of the variation in kinetic energies of the emitted species. The regions of lower kinetic energy in angular RPA measurements have provided a means to identify the origins of ion emission products as seen in Fig. 1. Since the IL jet structure only suffers from ohmic losses, then the emission products must be originating from the jet. The neck emission zone is close to the emitter where near zero ohmic losses occur in the cone, and thus ion emission products are near 500 eV. These observations have been restricted to IL emission from either etched metal needles or small capillaries with tip diameters less than 20  $\mu\text{m}$  [5,7,25,31].

Figure 10b illustrates the kinetic energy distributions of the ion emission products at an angle 17.5 deg from the center. The energy trends, except the 344 amu case, peak around 350 eV. For increasing IL flow rates, the kinetic energies of these species are reduced further

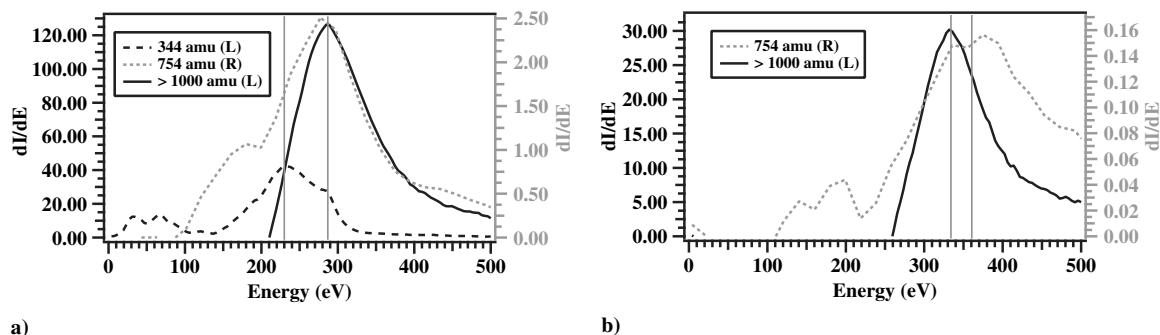


Fig. 10 RPA of plume at 0.27 nL/s a) 0 deg and b) 17.5 deg for 344 (left axis), 754 (right axis), and  $m/q > 1000$  amu (left axis).

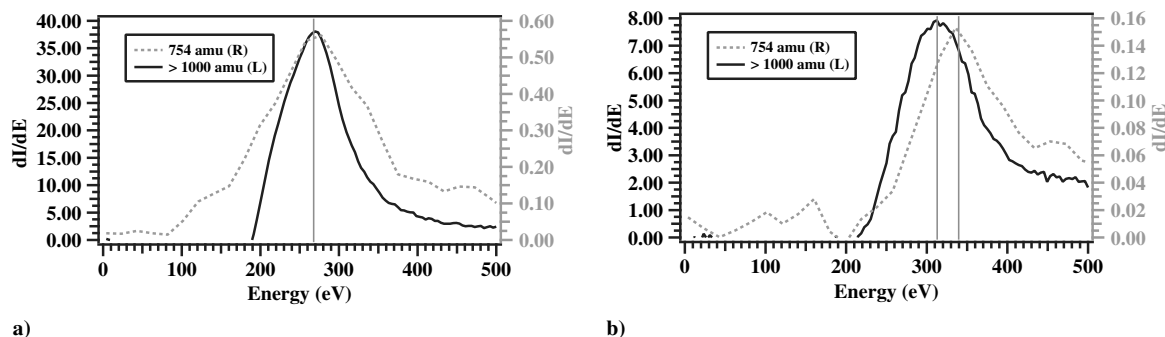


Fig. 11 RPA of plume at 1.24 nL/s a) 0 deg b) 1.75 deg for 754 and  $m/q > 1000$  amu.

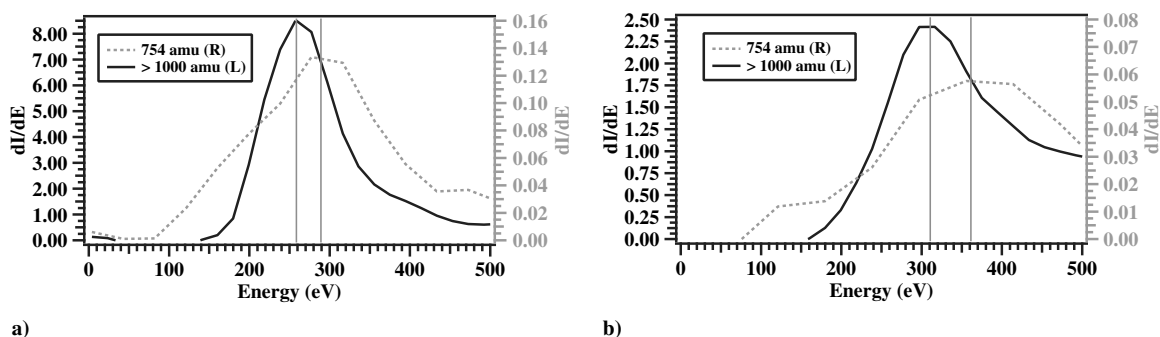


Fig. 12 RPA of plume at 2.18 nL/s a) 0 deg and b) 1.75 deg for 754 and  $m/q > 1000$  amu.

to approximately 330 eV in the cases of 1.24 and 2.18 nL/s of Figs. 11b and 12b. The on-axis plots (Figs. 10a, 11a, and 12a) show that the emission products of 754 and  $m/q > 1000$  amu undergo further reduction in kinetic energy. The peak energies are lower in this narrow region of the spray and are centered at approximately 270–290 eV. Based on the kinetic energy profiles, the large masses associated with  $m/q > 1000$  amu scans are the resulting products from the jet breakup. In Fig. 10a, the 344 amu energy profile is centered near the lower end of the  $m/q > 1000$  amu profile at approximately 230 eV. The profile suggests that the 344 amu species are predominately emitted from other sources, not from the jet breakup. If the 344 amu ions had originated from the same locations

as the larger mass emission products (e.g., the jet tip breakup), then the 344 amu energy distribution would be wider and centered on ~290 eV. The most likely source of the 344 amu emission products is field evaporation from the larger masses emitted from the jet breakup.

Table 2 [Bmim][DCA] cation species and associated masses for  $<1000$  amu

$n$ value	Cation	Mass, amu
0	Bmim <sup>+</sup>	139
1	Bmim([Bmim][DCA]) <sup>+</sup>	344
2	Bmim([Bmim][DCA]) <sub>2</sub> <sup>+</sup>	549
3	Bmim([Bmim][DCA]) <sub>3</sub> <sup>+</sup>	754
4	Bmim([Bmim][DCA]) <sub>4</sub> <sup>+</sup>	959

Table 3 Species percentage contribution to measured intensity

Flow rate, nL/s	Angle range, deg	Percentage of contribution to measured intensity				
		$n = 0$	$n = 1$	$n = 2$	$n = 3$	$n = 4$
0.27	0 to -30	10.9	56.5	21.6	7.4	3.7
0.49		1.5	2.4	42.6	32.6	20.9
0.72		2.0	1.3	38.2	35.6	22.9
1.24		6.1	1.4	33.5	35.3	23.8
2.18		11.2	1.8	18.0	28.3	40.7
0.27	-20 to -30	0.2	0.3	0.6	0.9	0.6
0.49		0.6	0.1	6.3	6.4	3.5
0.72		1.2	0.4	8.8	9.1	6.7
1.24		2.5	0.3	9.1	12.8	7.3
2.18		5.8	0.8	7.2	14.1	20.3

**Table 4** Current, mass flow rate ( $\dot{m}$ ), and mass-to-charge ratio ( $m/q$ ) data at select IL flow rates

Flow rate, nL/s	Integrated current, nA	Emitter current, nA	Current difference, %	Extractor current, nA	Integrated $\dot{m}$ , ng/s	Nominal $\dot{m}$ , ng/s	Integrated $m/q$ , amu	$I(Q)_{\text{beam}} m/q$ , amu
0.30	486	487	0.2	45	454	317	90,000	95,000
0.46	594	589	0.8	45	503	493	82,000	117,000
0.73	660	751	12.1	95	885	779.2	129,000	148,000
0.82	694	772	10.1	116	—	874	—	157,000
0.94	740	931	20.5	227	1590	1003	207,000	168,000
1.29	778	1032	24.6	342	2046	1369	254,000	197,000
1.45	777	1094	29.0	443	—	1539	—	209,000
1.82	749	1176	36.3	565	—	1937	—	234,000
2.18	740	1255	41.0	686	4335	2315	566,000	256,000

When the 344 amu products are emitted, the large masses have moved away from the jet and are at a lower potential. As a result, the 344 amu ions are at energies less than the parent large charged masses. The 754 amu profile shows this wider profile better than the 344 amu distribution. The 754 amu energy profile matches the large mass energies and suggests similar emission locations as these large masses. The 754 amu distribution does extend toward 100 eV as well. This extension suggests some of the 754 amu emission products are likely the result of field evaporation from larger charged masses as well.

The origins of the ion emission products conform to the typical emission zones of a cone-jet structure seen in Fig. 1, but with two caveats. First, the detected ion emission products are the result of a jet with a wide emission spray angle. Second, emission products from the neck are not reaching the detector. Instead, the neck emission products are establishing a second current path to the extractor. A wide-spraying jet is required to account for large mass species at high angles. Further investigation is needed to explain the mechanism behind the wide spray. The wide variation in the energy profiles of the RPA data would be the result of ion evaporation from the large masses (i.e., droplets) at points away from the jet structure. Emission products from the neck can be distinguished from the jet emission due to the exhibited kinetic energies of the ions and the ion masses associated with those energies. Neck emission tends to be low-mass ions, species  $n = 0$  to 2 as a result of field evaporation, and these ions have peak kinetic energies of  $\sim 500$  eV [3,4,7]. As a result, the neck emission products tend to be sources of charge, not mass. Based on the RPA results, these high-energy, low-mass ions are not present at any measured angle.

The near-field results listed in Table 4 for select IL flow rates justify the conclusion of where the emission products are originating. The integrated mass flow rate and current near-field data are proportionally different. The integrated mass flow from the jet emission approaches the nominal mass flow rate calculated from the IL density ( $1.063 \text{ g/cm}^3$ ) and volumetric flow rate. By the conservation of mass, the mass transmitted by the capillary must be emitted from the tip. The emitter current provides a measure of the current flow within the circuit before ion emission from the cone jet. If a substantial difference is observed between the integrated and emitter currents, then the current flow is being diverted into another circuit path instead of the path to the Faraday cup. The integrated current consistently represents 60 to 90% of the emitter current for IL flow rates over 0.90 nL/s (Fig. 8), and, subsequently, 10 to 40% of the current is recovered by the extractor. Assuming the emission products of the neck are low-mass ions, the percentage of the mass flux due to the extractor current can be determined. If any of the species of  $n = 0$  to 2 is assigned the extractor current, then the extractor mass flux represents less than 0.5% of the total mass flow rate detected. This means that near-field results represent near full mass flow rate collection but only partial charge collection for IL flow rates greater than 0.90 nL/s. The emitted current from the neck is being leaked to the extractor given the proximity to the capillary tip. Simion 8.1 software was used to model a cone-jet structure in a simple electrode configuration with a separation of 2 mm and singly charged ions emitted from the neck region. Simulation results showed, independent of ion mass, that ions from the neck did not reach the Faraday cup for detection and either impacted the extractor

or passed through the extractor aperture at an angle greater than 35 deg.

## B. Predicted Propulsion Performance

### 1. Beam Current and Mass Flow Rate

From the current data in Fig. 8, the empirical current scaling law  $I(Q)_{\text{beam}}$  can be determined by curve fitting to the data. This scaling law allows extrapolation of the emission output to flow rates not studied to be used in establishing potential propulsion performance at those flow rates. Electrospray scaling laws have been developed by Fernández de la Mora and Loscertales [29] [see Eq. (1)] and Gañán-Calvo et al. [30]. Those scaling laws were power functions with the constraint of zero current at zero flow rate. Equation (2) was derived by the same method using the combined measurements of the integrated current and extractor current and with the same constraint of zero current at zero flow rate as in [29,30]. The scaling law  $I(Q)_{\text{beam}}$  relates the current, in nanoamperes, and IL flow rate, in nL/s. Equation (2) is consistent with Eq. (1), developed by Fernández de la Mora and Loscertales. The curve fit establishes an equivalent power of 0.5. The scale factor of 986 can be broken down into values of  $f(\epsilon)$  and the IL physical properties (see Table 1). As a result,  $f(\epsilon)$  equates to 4.6 if the dielectric is assumed to be 11.3 [13]. This functional value is consistent with the results Fernández de la Mora and Loscertales established for the dielectric constant for pure solvents. The  $f(\epsilon)$  profile shows that when  $\epsilon = 10$ ,  $f(\epsilon) = 4$  [29].

In addition, a linear fit [Eq. (3)] was applied to the integrated mass flow rate since the measurement exceeded the nominal rates based on the IL density and volumetric rate. The minimum current can be calculated using the minimum IL flow rate in Eq. (4) as determined by Fernández de la Mora [32] and evaluated in Eq. (2). At the minimum flow rate of 4.35 picoliters per second (pL/s), which is much less than the range studied, the minimum current value is 65 nA. The minimum IL flow rate is larger than the required rate of 0.09 pL/s needed to overcome the hydraulic resistance of the capillaries. For this investigation, the minimum IL flow is only used to define a theoretical lower limit of the scaling law:

$$I(Q) = f(\epsilon) \cdot \left[ \frac{\gamma K Q}{\epsilon} \right]^{0.5} \quad (1)$$

$$I(Q)_{\text{beam}} = 986 \cdot Q^{0.5} \quad (2)$$

$$\dot{m} = 1770 \cdot Q \quad (3)$$

$$Q_{\text{min}} = \frac{\gamma \epsilon \epsilon_0}{\rho K} \quad (4)$$

The emitted current and mass flow rate are required quantities needed to calculate the mass-to-charge ratio  $m/q$  output at each IL flow rate. Table 4 lists the various values of current, mass flow rate, and  $m/q$  output. The current data indicate a 10 to 41% loss in the integrated current measurement at mid to high IL flow rates, but this is recovered as a current on the extractor electrode. The current loss is translated to the  $m/q$  value calculated using the integrated current and mass flow rate data. The integrated mass-to-charge ratio is 1.5 times higher than

**Table 5** Predicted propulsion performance of a single electrospray emitter operating on [Bmim][DCA] at select IL flow rates

IL flow rate, nL/s	Full $q/m$ , C/kg	Full thrust, $\mu\text{N}$	Axial $q/m$ , C/kg	Axial thrust, $\mu\text{N}$	Cosine thrust loss, %	$I_{sp}$ , s	Emission power, mW
0.30	1071	0.89	1059	0.84	5.7	200	0.87
0.46	1180	1.03	1146	0.96	6.8	210	1.06
0.73	745	1.45	726	1.32	8.8	167	1.18
0.94	465	2.05	458	1.83	11.2	132	1.33
1.29	380	2.39	370	2.10	12.0	119	1.39
2.18	171	3.39	167	2.90	13.0	80	1.33

the mass-to-charge ratio determined from the results of the current fit in Eq. (2) and mass flow rate fit in Eq. (3) referred to as  $I(Q)_{\text{beam}}$  in Table 4.

## 2. Determination of Thrust and $I_{sp}$

The propulsion performance of a single emitter is predicted using the collected current density and mass flow rate data. Six IL flow rates (see Table 5) are selected to study the performance of the emitter output under variable IL flow rate conditions. These IL flow rates are selected based on the available mass flow rate data collected. Calculations of thrust  $I_{sp}$  and power required are determined using Eqs. (5–7). Only the total thrust of the electrospray beam, not the thrust provided by each ion species, can be determined. Since the percentage of droplet contribution cannot be determined, it would be inappropriate to use the percentages reported in Table 3 as the droplet contribution would be completely neglected. For the calculation of thrust [Eq. (5)], the acceleration potential  $V_{\text{acc}}$  is required, but this value actually depends on the ohmic losses occurring within the electrospray beam as the IL flow rate changes. For simplification, a standard value of 1793 V is used in all the following calculations. The ohmic loss value used to determine  $V_{\text{acc}}$  is established by averaging the losses of the peak kinetic energies for both the on and off axes in the RPA results of  $m/q > 1000$  amu:

$$F = \dot{m}v = \dot{m} \sqrt{\frac{2V_{\text{acc}}q}{m}} = \sqrt{2V_{\text{acc}}\dot{m}I} \quad (5)$$

$$I_{sp} = \frac{F}{\dot{m}g} \quad (6)$$

$$P_e = IV_{\text{acc}} \quad (7)$$

Table 5 lists the propulsion performance of the [Bmim][DCA] capillary emitter at the six selected flow rates. The full thrust value uses the integrated beam current and mass flow rate values in Table 4 with no correction for cosine losses. The axial thrust value takes into account cosine losses and is a true representation of the thrust contribution from the emitted products detected by the near-field sensors. Within the detection range of  $\pm 60^\circ$  deg, the cosine loss is less than 13% for up to a flow of 2.18 nL/s. The specific charge  $q/m$  used to determine these two sets of thrust values is also listed in Table 5 for comparison. At 0.30 nL/s, the axial thrust output is

0.84  $\mu\text{N}$  with an  $I_{sp}$  of 200 s. Increasing the IL flow rate to 2.18 nL/s increases the thrust output to 2.90  $\mu\text{N}$  with an  $I_{sp}$  of 80 s. The increasing of the IL flow rate results in nearly doubling the thrust output of the single emitter. The impact of charged droplet contributions can be seen in the  $I_{sp}$  value. The large mass contributions of the droplets reduce the  $I_{sp}$  of the emitter to nearly 100 s.

Better performance would be achieved above 0.90 nL/s with a minimized extractor current path. To that end, an empirical set of thrust and  $I_{sp}$  data have been determined and are presented as well. Unlike the data in Table 5, the empirical results derived from Eqs. (2) and (3) do not account for cosine losses and only reflect a theoretical full thrust output. The empirical performance predictions of a single emitter are shown in Fig. 13 for a IL flow rate of 4.35 pL/s up to 2.5 nL/s. The results of Table 5 reflect zero contribution from the extractor current and indicate that the emission products from the jet structure drive the performance of the electrospray emitter at the investigated flow rate range. However, the undetected emission at a high angle does affect the performance and operational efficiency of the electrospray emitter. For the electrode configuration operated at below 0.9 nL/s, the results of Table 5 and of Fig. 13 provide the clear propulsion performance of a [Bmim][DCA] electrospray emitter. The maximum thrust achievable is approximately 1.83  $\mu\text{N}$  with an  $I_{sp}$  of 132 with a beam divergence limited to less than  $\pm 50^\circ$  deg based on near-field data. Operating the electrospray emitter above 0.90 nL/s will result in limited thrust gains and the IL contamination of the extractor.

## V. Conclusions

From the [Bmim][DCA] results, there will be tradeoffs in electrospray performance when the IL flow rate is adjusted to vary propulsive output. Based on the mass spectra collected, the electrospray beam is composed of a mix of ions ( $\text{Bmim}([\text{Bmim}][\text{DCA}])_n^+$ ;  $n = 0-4$ ) and charged droplets for the IL flow rate range studied. When the IL flow rate is increased, the droplet contribution begins to dominate the beam composition. This droplet domination leads to increased thrust, but with a penalty in efficient use of the IL propellant (i.e., decreased  $I_{sp}$ ). For the [Bmim][DCA] 50  $\mu\text{m}$  ID emitter as configured, angled-resolved near-field measurements indicate the IL flow rate should be limited to a maximum of 0.90 nL/s to maximize the specific charge and to avoid establishing an extractor path. At these low flow rates the beam divergence remains under  $\pm 50^\circ$  deg. In reducing the flow rate, the electrospray beam composition will shift toward pure ionic contributions, and increased  $q/m$  ratios will be established at a low angle. Operating above 0.90 nL/s will result in the acceleration of 99% of the emitted IL mass, but only a proportion of the total charge input will contribute due to the presence of the extractor current. At 0.90 nL/s, the thrust and  $I_{sp}$  are 1.83  $\mu\text{N}$  and 132 s, respectively. Increasing the IL flow rate to 2.18 nL/s only achieves an additional 1.07  $\mu\text{N}$  of thrust at 80 s  $I_{sp}$ .

The data suggest minimizing the current loss to the extractor from the neck of the Taylor cone and ohmic losses along the jet structure. The current loss impacts the calculated propulsion output of the emitter, and such values do not truly reflect the performance of the emitter. Adjustment to the experimental setup, such as reducing electrode spacing and increasing the diameter of the extractor aperture, should ensure reduced current loss and allow additional emission product to reach the detectors. Ohmic losses are inherent to electrospray systems due to the size of the jet structure and properties of the electrospray propellant. Minimizing ohmic losses ensures

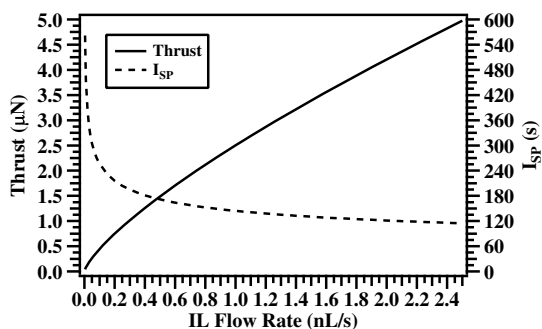


**Fig. 13** Predicted propulsion performance of a single electrospray emitter based on the empirical current scaling law of Fig. 8.

energetic emission products and can only be achieved by controlling the size of the jet. Overall, the data show that the IL flow rate can be adjusted to change performance just as well as the beam current through voltage variation. Flow rate adjustment does not require a robust electrical system to handle higher voltages (3–20 kV).

### Acknowledgments

This work was supported by Air Force Office of Scientific Research under task number 2303EP02 (Program Manager: M. Berman) and number 13RV07COR (Program Manager: A. Sayir).

### References

- [1] Taylor, G. I., "Disintegration of Water Drops in an Electric Field," *Proceedings of the Royal Society of London, Series A: Mathematical and Physical Sciences*, Vol. 280, No. 1382, 1964, pp. 383–397. doi:10.1098/rspa.1964.0151
- [2] Iribarne, J. V., and Thomson, B. A., "On the Evaporation of Small Ions from Charged Droplets," *Journal of Chemical Physics*, Vol. 64, No. 6, 1976, pp. 2287–2294. doi:10.1063/1.432536
- [3] Gamero-Castaño, M., and Fernandez de la Mora, J., "Direct Measurement of Ion Evaporation Kinetics from Electrified Liquid Surfaces," *Journal of Chemical Physics*, Vol. 113, No. 2, 2000, pp. 815–832. doi:10.1063/1.481857
- [4] Gamero-Castaño, M., "Electric-Field-Induced Ion Evaporation from Dielectric Liquid," *Physical Review Letters*, Vol. 89, No. 14, 2002, pp. 147602-1–147602-4. doi:10.1103/PhysRevLett.89.147602
- [5] Chiu, Y., Gaeta, G., Heine, T. R., Dressler, R. A., and Lavandier, D. J., "Analysis of the Electrospray Plume from the EMI-Im Propellant Externally Wetted on a Tungsten Needle," *42nd AIAA/ASME/SAE/ASEE Joint Propulsion Conference and Exhibit*, AIAA Paper 2006-5010, 2006.
- [6] Romero-Sanz, I., Bocanegra, R., Fernandez de la Mora, J., and Gamero-Castaño, M., "Source of Heavy Molecular Ions Based on Taylor Cones of Ionic Liquids Operating in the Pure Ion Evaporation Regime," *Journal of Applied Physics*, Vol. 94, No. 5, 2003, pp. 3599–3605. doi:10.1063/1.1598281
- [7] Chiu, Y., and Dressler, R. A., "Ionic Liquids for Space Propulsion," *Ionic Liquids IV: Not Just Solvents Anymore*, American Chemical Soc., Washington, D.C., 2007, pp. 138–161.
- [8] Schreiner, C., Zugmann, S., Hartl, R., and Gores, H. J., "Fractional Walden Rule for Ionic Liquids: Examples from Recent Measurements and a Critique of the So-Called Ideal KCl Line for the Walden Plot," *Journal of Chemical and Engineering Data*, Vol. 55, No. 5, 2009, pp. 1784–1788. doi:10.1021/jc900878j
- [9] Miller, S. W., Prince, B. D., and Rovey, J. L., "Capillary Extraction of the Ionic Liquid [Bmim][DCA] for Variable Flow Rate Operations," *48th AIAA/ASME/SAE/ASEE Joint Propulsion Conference and Exhibit*, AIAA Paper 2012-3738, 2012.
- [10] Zech, O., Stoppa, A., Buchner, R., and Kunz, W., "The Conductivity of Imidazolium-Based Ionic Liquids from (248 to 468) K. B. Variation of the Anion," *Journal of Chemical and Engineering Data*, Vol. 55, No. 5, 2010, pp. 1774–1778. doi:10.1021/jc900793r
- [11] Carvalho, P. J., Regueira, T., Santos, L. M. N. B. F., and Coutinho, J. A. P., "Effect of Water on the Viscosities and Densities of 1-Butyl-3-Methylimidazolium Dicyanamide and 1-Butyl-3-Methylimidazolium Tricyanomethane at Atmospheric Pressure," Vol. 55, No. 2, 2010, pp. 645–652. doi:10.1021/jc900632q
- [12] Sánchez, L. G., Espel, J. R., Onink, F., Meindersma, G. W., and de Haan, A. B., "Density, Viscosity, and Surface Tension of Synthesis Grade Imidazolium, Pyridinium, and Pyrrolidinium Based Room Temperature Ionic Liquids," *Journal of Chemical and Engineering Data*, Vol. 54, No. 10, 2009, pp. 2803–2812. doi:10.1021/jc800710p
- [13] Stoppa, A., Hunger, J., Buchner, R., Hefter, G., Thoman, A., and Helm, H., "Interactions and Dynamics in Ionic Liquids," *Journal of Physical Chemistry B*, Vol. 112, No. 16, 2008, pp. 4854–4858. doi:10.1021/jp800852z
- [14] Wandschneider, A., Lehmann, J. K., and Heintz, A., "Surface Tension and Density of Pure Ionic Liquids and Some Binary Mixtures with 1-Propanol and 1-Butanol," *Journal of Chemical and Engineering Data*, Vol. 53, No. 2, 2008, pp. 596–599. doi:10.1021/jc700621d
- [15] Weingärtner, H., "The Static Dielectric Constant of Ionic Liquids," *Zeitschrift für Physikalische Chemie*, Vol. 220, No. 10, 2006, pp. 1395–1405. doi:10.1524/zpch.2006.220.10.1395
- [16] Berg, S. P., "Design and Development of Ionic Liquid Dual-Mode Spacecraft Propellants," Masters Thesis, Mechanical and Aerospace Engineering Dept., Missouri Univ. of Science & Technology, Rolla, MO, 2012.
- [17] Schneider, S., Hawkins, T., Rosander, M., Vaghjiani, G., Chambreau, S., and Drake, G., "Ionic Liquids as Hypergolic Fuels," *Energy and Fuels*, Vol. 22, No. 4, 2008, pp. 2871–2872. doi:10.1021/ef800286b
- [18] Berg, S. P., and Rovey, J. L., "Dual-Mode Propellant Properties and Performance Analysis of Energetic Ionic Liquids," *50th Aerospace Sciences Meeting*, AIAA Paper 2012-0975, 2012.
- [19] Berg, S. P., and Rovey, J. L., "Assessment of Imidazole-Based Ionic Liquids as Dual-Mode Spacecraft Propellants," *Journal of Propulsion and Power*, Vol. 29, No. 2, 2013, pp. 339–351. doi:10.2514/1.B34341
- [20] Donius, B. R., and Rovey, J. L., "Ionic Liquid Dual-Mode Spacecraft Propulsion Assessment," *Journal of Spacecraft and Rockets*, Vol. 48, No. 1, 2011, pp. 110–123. doi:10.2514/1.49959
- [21] Donius, B. R., and Rovey, J. L., "Analysis and Prediction of Dual-Mode Chemical and Electric Ionic Liquid Propulsion Performance," *48th Aerospace Sciences Meeting*, AIAA Paper 2010-1328, 2010.
- [22] Cloupeau, M., and Prunet-Foch, B., "Electrostatic Spraying of Liquids in Cone-Jet Mode," *Journal of Electrostatics*, Vol. 22, No. 2, 1989, pp. 135–159. doi:10.1016/0304-3886(89)90081-8
- [23] Gamero-Castaño, M., and Hruby, V., "Electrospray as a Source of Nanoparticles for Efficient Colloid Thrusters," *Journal of Propulsion and Power*, Vol. 17, No. 5, 2001, pp. 977–987. doi:10.2514/2.5858
- [24] Chiu, Y., Levandier, D., Austin, B., Dressler, R. A., Murray, P. T., Lozano, P., and Martinez-Sanchez, M., "Mass Spectrometric Analysis of Ion-Emission from Selected Colloid Thruster Fuels," *39th AIAA/ASME/SAE/ASEE Joint Propulsion Conference and Exhibit*, AIAA Paper 2003-4848, 2003.
- [25] Chiu, Y., Gaeta, G., Levandier, D. J., Dressler, R. A., and Boatz, J. A., "Vacuum Electrospray Ionization Study of the Ionic Liquid, [Emim][Im]," *International Journal of Mass Spectrometry*, Vol. 265, Nos. 2–3, 2007, pp. 146–158. doi:10.1016/j.ijms.2007.02.010
- [26] Lozano, P. C., "Studies on the Ion-Droplet Mixed Regime in Colloid Thrusters," Ph.D. Dissertation, Aeronautics and Astronautics Dept., Massachusetts Inst. of Technology, Cambridge, MA, 2003.
- [27] Ticknor, B. W., Anderson, J. K., Fritz, B. A., and Chiu, Y.-H., "Effect of Aspect Ratio on the Wettability and Electrospray Properties of Porous Tungsten Emitters with the Ionic Liquid [Emim][Im]," *46th AIAA/ASME/SAE/ASEE Joint Propulsion Conference and Exhibit*, AIAA Paper 2010-6618, 2010.
- [28] Manzella, D. H., and Sankovic, J. M., "Hall Thruster Ion Beam Characterization," *31st AIAA/ASME/SAE/ASEE Joint Propulsion Conference and Exhibit*, AIAA Paper 1995-2927, 1995.
- [29] Fernández de la Mora, J., and Loscertales, I. G., "The Current Emitted by Highly Conducting Taylor Cones," *Journal of Fluid Mechanics*, Vol. 260, No. 1, 1994, pp. 155–184. doi:10.1017/S0022112094003472
- [30] Gañán-Calvo, A. M., Dávila, J., and Barrero, A., "Current and Droplet Size in the Electrospraying of Liquids. Scaling Laws," *Journal of Aerosol Science*, Vol. 28, No. 2, 1997, pp. 249–275. doi:10.1016/S0021-8502(96)00433-8
- [31] Ticknor, B. W., Miller, S. W., and Chiu, Y. H., "Mass Spectrometric Analysis of the Electrospray Plume from an Externally Wetted Tungsten Ribbon Emitter," *45th AIAA/ASME/SAE/ASEE Joint Propulsion Conference and Exhibit*, AIAA Paper 2009-5088, 2009.
- [32] Fernández de la Mora, J., "On the Outcome of the Coulombic Fission of a Charged Isolated Drop," *Journal of Colloid and Interface Science*, Vol. 178, No. 1, 1996, pp. 209–218. doi:10.1006/jcis.1996.0109

A. Gallimore  
Associate Editor

## **DISTRIBUTION LIST**

DTIC/OCP

8725 John J. Kingman Rd, Suite 0944  
Ft Belvoir, VA 22060-6218

1 cy

AFRL/RVIL

Kirtland AFB, NM 87117-5776

2 cys

Official Record Copy

AFRL/RVBXT/Dr. Raymond Bemish

1 cy

This page is intentionally left blank.